Egypt. J. Chem. **Vol. 67**, No. 1 pp. 125 - 140 (2024)

Egyptian Journal of Chemistry

http://ejchem.journals.ekb.eg/

Photocatalytic Degradation of Fluorescein Dye through SnS_2/SnO_2 Photocatalyst for Efficient Environmental Remediation

Saddam A. Alaskary[a], M.F. El-Shahat[b], M.A. Ahmed[b], Maryam G. Elmahgary[a,c*]*

[a]Department of Chemical Engineering, The British University in Egypt, Cairo, Egypt

[b] Chemistry Department, Faculty of Science, Ain Shams University, Cairo, Egypt

[c] *Department of Chemical Engineering, Massachusetts Institute of Technology, 77 Massachusetts A Cambridge, MA 02139, USA*

Abstract

The SnS_2/SnO_2 nanocomposite, employed as a photocatalyst for the photodegradation of fluorescein dye, demonstrates the significant role of mass ratio and catalyst dosage in photocatalytic degradation. The relatively small disparity between the conduction bands of SnS_2 (E_{CB} = -0.895 eV) and SnO_2 (E_{CB} = 0.15 eV) is conducive for the formation of a Z-scheme, which curbs the recombination process and elevates photocatalytic activity. The nanocatalyst was synthesized using the sol-gel method and subsequently characterized through XRD, SEM, TEM, EDX, mapping, DRS, and XPS. The peak intensity of the photoluminescence (PL) study, relating to the optical property of the catalyst, was observed at 829 nm. The efficacy of the prepared SnS_2/SnO_2 nanoparticles against photostable fluorescein dye (Flu) photodegradation was evaluated, showing a 77.67% reduction in fluorescein dye within 240 minutes at a p^H level of 7. Additionally, the recyclability study affirmed the stability of the catalyst over four successive runs.

Keywords: SnS_2; SnO_2; Photodegradation; fluorescein dye; sol-gel.

1. Introduction

The discharge of wastewater into the environment can generate substantial environmental concerns and pose risks to human health [1]. Consequently, there is a pressing need to identify efficient solutions for treating organic dye effluent. Various methods, such as adsorption [2], biological treatment [3], precipitation-coagulation [4], membrane processes, advanced oxidation [5-8], ultrafiltration, dialysis, electrodialysis [9, 10], reverse osmosis [11, 12], and photocatalytic degradation have been explored. Recently, photocatalytic degradation has emerged as a successful, cost-effective approach to remove dyes. Of the techniques available, photocatalytic technology, which harnesses solar energy, stands out as the most promising. However, the presence of organic pollutants that can transform into harmful chemicals in wastewater through hydrolysis, oxidation, or other chemical reactions, makes the removal of these toxic compounds a challenging task [13]. Tin oxide (SnO_2) is recognized for its photocatalytic prowess in the photodegradation of organic molecules [14], making it a significant semiconductor material, superior to other photocatalysts like TiO_2, ZnO, CdS. Attributes such as low cost, non-toxicity, high activity, vast chemical stability, limited water solubility, and eco-friendly properties have bolstered its appeal [15, 16]. SnS_2, a visible light-active sulphide photocatalyst with a narrow band gap (E_g = 1.9–2.3 eV), inhibits charge carrier recombination. Coupled with its strong physicochemical stability and low toxicity, it's an attractive material for metal-sulphide-metal oxide heterojunction-based photocatalysts. Its photocatalytic activity can be enhanced by modulating morphologies like nanoplates, nanoflakes, nanosheets, nanotubes, nanoflowers, and nanorods. Notwithstanding its impressive properties,

*Corresponding author e-mail: maryam.galal@bue.edu.eg

Receive Date: 16 October 2022, Revise Date: 25 May 2023, Accept Date: 01 July 2023

DOI: 10.21608/EJCHEM.2023.168614.7096

virgin SnS_2 displays weak photocatalytic activity due to rapid charge carrier recombination and photocorrosion [17].

The study focuses on SnS_2/SnO_2 heterostructures using SnS_2 coupling to augment light absorption and the rate of photogenerated carrier separation via a one-pot solid-state technique. The photocatalytic performance of these heterostructures was found to be significantly superior to pure SnO_2. In the degradation of Eriochrome Black T, SnO_2-nanoparticles showed a 35.9% efficiency [18]. The photocatalytic activity of newly synthesized SnO_2 nanoparticles was evaluated for the degradation of two organic dyes, methylene blue (MB) and Eriochrome Black-T (EBT), achieving excellent efficiencies of approximately 90% and 83%, respectively [19]. Furthermore, SnO_2 quantum dots (2–10 nm) hybridized with a crucial two-dimensional semiconductor, graphene-like g-C_3N_4, were used as catalysts for photocatalytic breakdown of organic molecules, specifically Rhodamine B. They displayed remarkably enhanced photocatalytic activity, with up to 95% degradation for RhB in 60 minutes [20]. For the photocatalytic degradation of fluorescein dye (FLU), highly mesoporous $AgIO_4$/g-C_3N_4 nanoparticles were deployed, achieving an impressive removal rate of 98% [21]. A novel hybrid photocatalyst, SnS_2 on SnO_2, has been prepared by the sol-gel method for photodegrading fluorescein dye under UV radiation. This SnS_2/SnO_2 composite was characterized using X-ray diffraction (XRD), scanning electron microscopy (SEM), photoluminescence (PL), energy dispersive X-ray (EDX), diffuse reflectance spectra (DRS), Brunauer-Emmett-Teller (BET) surface area analysis, and X-ray photoelectron spectroscopy (XPS).

2. Experimental

2.1. Materials

The chemicals used in this study included stannic chloride pentahydrate ($SnCl_4.5H_2O$), sodium sulfide nonahydrate ($Na_2S.9H_2O$), ammonium hydroxide (NH_4OH), CTAB (Cetrimide), ammonium acetate, silver nitrate ($AgNO_3$), p-benzoquinone, disodium dioxalate, terephthalic acid, and fluorescein dye. All these chemicals were of pure grade and were utilized without any further purification. All solutions were prepared using double-distilled water.

2.2 Preparation of SnO_2

The SnO_2 nanoparticles were synthesized utilizing the sol-gel technique. Initially, 20 g of stannic chloride was combined with 250 mL of distilled water. Subsequently, 20 mL of CTAB solution, prepared by diluting 3 g of CTAB in 50 mL of hot water, was added to the mixture. This was followed by continuous stirring for an hour, after which an ammonia solution was incrementally introduced drop by drop until complete precipitation was realized. The concoction was then stirred for an additional 2 hours, filtered, and thoroughly washed to remove all chloride ions. Finally, the product was dried at 100 °C and calcined at 500 °C for a duration of 2 hours.

2.3 Preparation of SnS_2

To the procedure, 10 g of stannic chloride was introduced to 100 mL of distilled water. Subsequently, 1 M sodium sulfide was added gradually until complete precipitation was observed. The mixture was then agitated for 2 hours, filtered, and thoroughly washed to remove all remaining chloride ions.

2.4. Preparation of SnS_2 on SnO_2 in Situ

SnO_2 and $SnCl_4.5H_2O$ were combined with 50 mL of distilled water and stirred continuously for one hour. Then, 1M sodium sulfide was gradually introduced until precipitation was complete. After stirring the solution for an additional two hours, it was filtered and subsequently dried to obtain SnS_2 on SnO_2. This process was repeated to prepare various concentrations of SnS_2 on SnO_2.

3. Results and discussions

3.1. Physiochemical characterization

3.1.1. XRD measurement

The crystalline phase of the prepared photocatalyst was identified using X-ray diffraction (XRD) within the 2θ range of 0–90 degrees. The XRD patterns for SnO_2 nanoparticles were displayed in Fig 1 to pinpoint the crystalline structure of the sample [22] [23]. Multiple peaks were detected at 2θ values of 26.5541°, 33.8156°, 37.9231°, 38.9106°, 51.7546°, 54.6488°, 57.7825°, 61.9193°, 64.6941°, 65.9417°, 71.2843°,78.6553°, 83.6734° and 87.3498°, which correspond to the Miller indices (110), (101), (200), (111), (211), (220), (002), (310), (112), (301), (202), (321), (222), and (330). These results unveiled the existence of the SnO_2's tetragonal structure (Space group: P42/mnm) and the reference code: 01-077-0448.

The XRD patterns for SnS_2 showcased several peaks illustrated in Fig1 at 2θ values of 14.2410, 28.0312, 33.6523, 45.7570, 50.8543, 52.8308, 57.5171, 61.0249, 64.4178, 66.6158, and 83.2410. These values correspond to the Miller indices (111), (311), (400), (511), (440), (531), (533), (622), (711), (711), and (840), which confirmed the cubic structure of SnS_2 (Space group: Fd-3m) and the reference code: 01-083-6036. Regarding the SnS_2/SnO_2 nanoparticles, the XRD patterns for 5%

SnS_2/SnO_2 exhibited several peaks depicted in Fig 1 with the space group P42/mnm and reference code 01-077-3163. Meanwhile, the 8% SnS_2/SnO_2 XRD patterns had multiple peaks shown in Fig 1 with the space group P-3m and reference code 01-084-9290 for SnS_2. The 10% SnS_2/SnO_2 XRD patterns demonstrated several peaks in Fig 1, with the space group P-31m and reference code 01-083-1707 for SnS_2. Lastly, the XRD patterns for 15% SnS_2/SnO_2 displayed several peaks in Fig 1 with space groups P42/mnm (reference code 01-070-6995) for SnO_2 and P-31m (reference code 01-084-9296) for SnS_2. The major phase was represented by the (110), (101), and (211) phases.

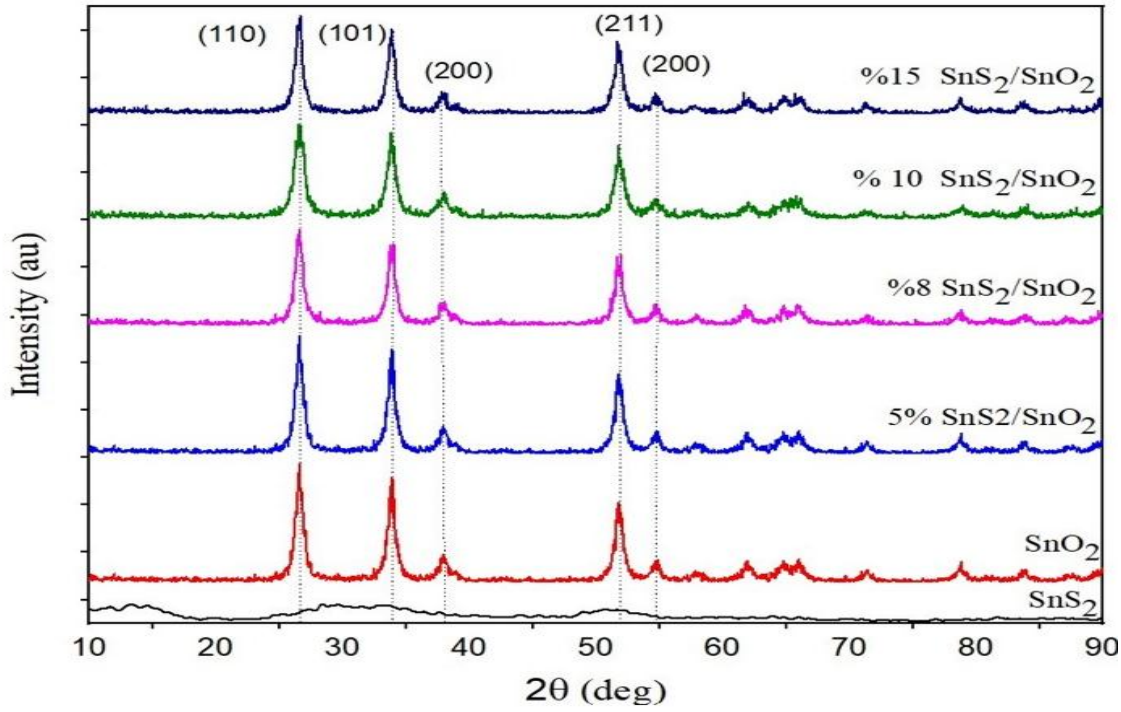

Fig 1: XRD FOR SnO_2, SnS_2 and different portions of SnS_2/SnO_2

3.1.2. Morphology of photocatalyst

The texture and morphology of many nanocatalysts play crucial roles in material properties, greatly influencing the nanocrystal size and shape's impact on photocatalytic activity. Based on the Scanning Electron Microscopy (SEM) analysis of the photocatalyst matrix, it was observed that the SnO_2 displayed an evident spheroidal shape, as illustrated in Fig. 2(a). On the other hand, SnS_2 presented irregular crystals, as depicted in Fig. 2(b). A composite of SnS_2/SnO_2 was then produced, as demonstrated in Fig. 2(c). Transmission Electron Microscopy (TEM)further revealed the nanostructure of the composite, as shown in Fig. 2(d), with an average particle size of 10 nm.The Selected Area Electron Diffraction (SAED) pattern displays highly bright rings, indicative of well-aligned and regular nanocrystals, as depicted in Fig. 2(e). The nitrogen adsorption-desorption isotherm at 77 K shows a very small uptake in the p/po range of 0.1–0.9, with a sharp increase upon reaching 1, as illustrated in Fig. 2(f). This suggests the presence of a minor group of pores, with a volume of 7.97 x 10-3 cm3/g and a surface area of 1.01726 m^2/g for SnS_2, as calculated using the Brunauer-Emmett-Teller (BET) equation. This material is characteristically nonporous and follows a type-II adsorption isotherm. The isotherm displays a minimal uptake in the p/po range of 0.1–0.7, followed by a substantial increase from p/po = 0.7 to 0.9, then a plateau and a sharp rise upon reaching 1, as depicted in Fig. 2(g). This reflects the presence of a minor group of pores, with a volume of 0.1007 cm^3/g and a surface area of 25.9 m^2/g for SnO_2, as calculated using the BET equation. The characteristic material is mesoporous and adheres to a type-II adsorption isotherm. As shown in Fig. 2(h), the 10% SnS_2/SnO_2 follows a type-II adsorption isotherm, with a surface area of 29.7 m^2/g and a pore volume of 0.1153 cm^3/g. The catalyst is identified as mesoporous [25][26][27].

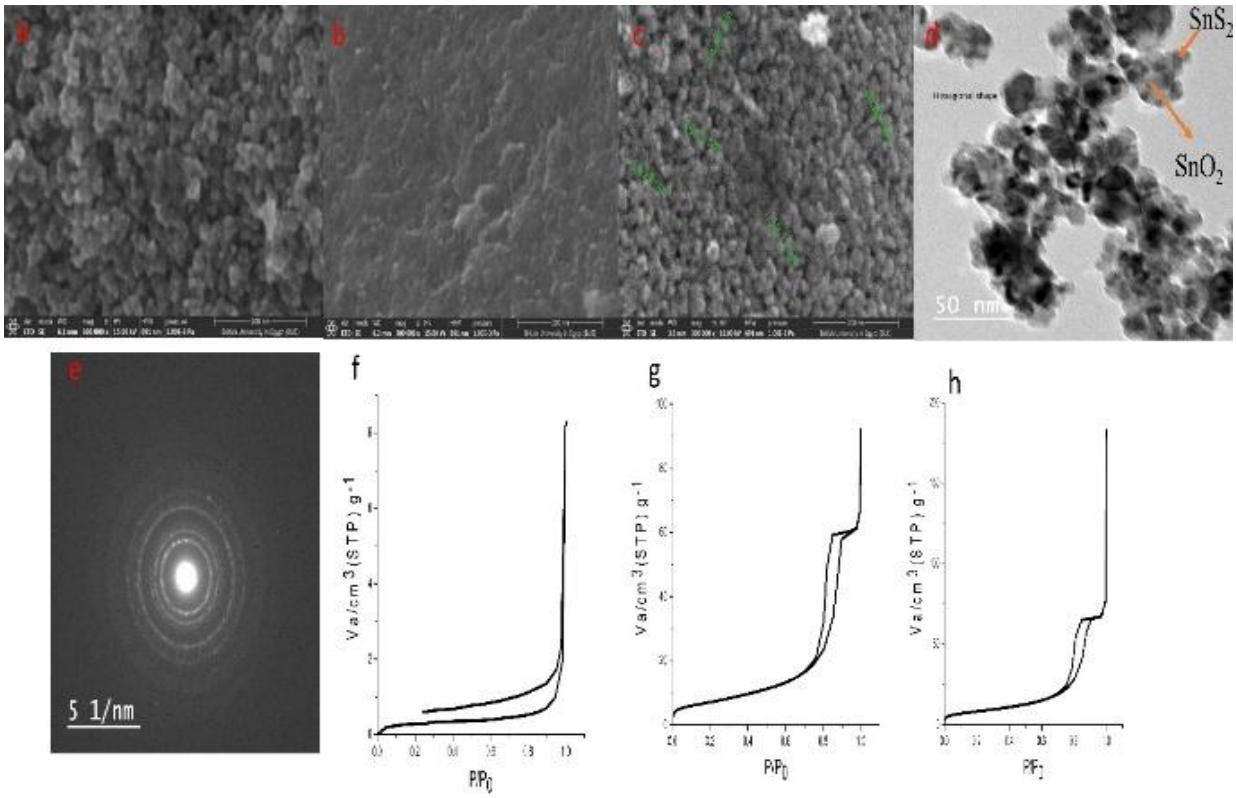

Fig 2: SEM image (a) for SnO2 ,(b) for SnS_2, (c) for 10 % SnS_2/SnO_2, (d) TEM image, (e) SAED of SnS_2/SnO_2, (f) N_2 adsorption-desorption isotherm for SnS_2, (g) for SnO2 and (h) for 10 % SnS_2/SnO_2.

3.1.3. Optical properties

Diffuse Reflectance Spectroscopy (DRS) is an essential technique for characterizing the absorption profile and optical properties of nanoparticles. Furthermore, it facilitates the determination of band gaps via the Tauc equation, as given by eq. (1) [28].

$$\propto(h\nu) = B\ (h\nu - Eg)^{n} \quad (1)$$

For an indirect allowed transition, it is plotted as (αhν)^(1/2) versus E with n = 2. For a direct allowed transition, it is plotted as (αhν)^2 versus E with n = 1/2. In these equations, Eg represents the band gap (in eV), h is Planck's constant (in J.s), B is the absorption constant, υ is the light frequency (in s^{-1}), and α is the extinction coefficient. The energy E is computed using Eq. (2).

When a composite is formed between SnS_2 and SnO_2, the band gap decreases slightly, as depicted in Fig. 5(a).

$$E = h\nu = hc/\lambda = 1240/\lambda \quad (2)$$

Terephthalic acid (TA) is used as a probe for the photoluminescence detection of hydroxyl radical production, as it exhibits excitation at 315 nm as illustrated in Fig. 3(b). The advantage of using TA lies in its structural symmetry, which allows only 2-hydroxyterephthalic acid (TAOH) to be identified as a product of hydroxylation [29].

3.2. Chemical composition

EDX and selected area mapping analyses confirmed the presence of elements in SnO_2, SnS_2, and SnS_2 on SnO_2. The EDX spectrum, as depicted in Fig. 4(a), specifies the presence and quantities of Oxygen (O), Sulphur (S), and Tin (Sn) elements in the SnS_2/SnO_2 composite, thereby corroborating the existence of all components within the composite. The individual mapping of these elements and the SnS_2/SnO_2 composite are illustrated in Fig. 4 (b–e), which validates their presence. XPS is an efficient method for determining the oxidation states of produced sample constituents. All detected peaks in Fig. 5(a) signified the presence of Sn, O, and a trace of Carbon (C), with the peaks observed at 487.83 and 532 eV corresponding to Sn (3d) and O (1s), respectively. Carbon, abundant on all surfaces, is typically seen in XPS spectra. The Carbon C 1s peak at 286.0 eV is often used as a charge correction reference. As seen in Fig. 5(b), Sn(3d) showcases two distinct peaks at 486.88 and 495.38 eV. The 8.5 eV energy difference between these peaks verifies the formation of the Sn^{4+} oxidation state in SnO2 [30] [31] [32].

Fig 3:(a) DRS of SnO_2, SnS_2 and different composites of SnS_2/SnO_2 and (b) Photoluminescence for terephthalic.

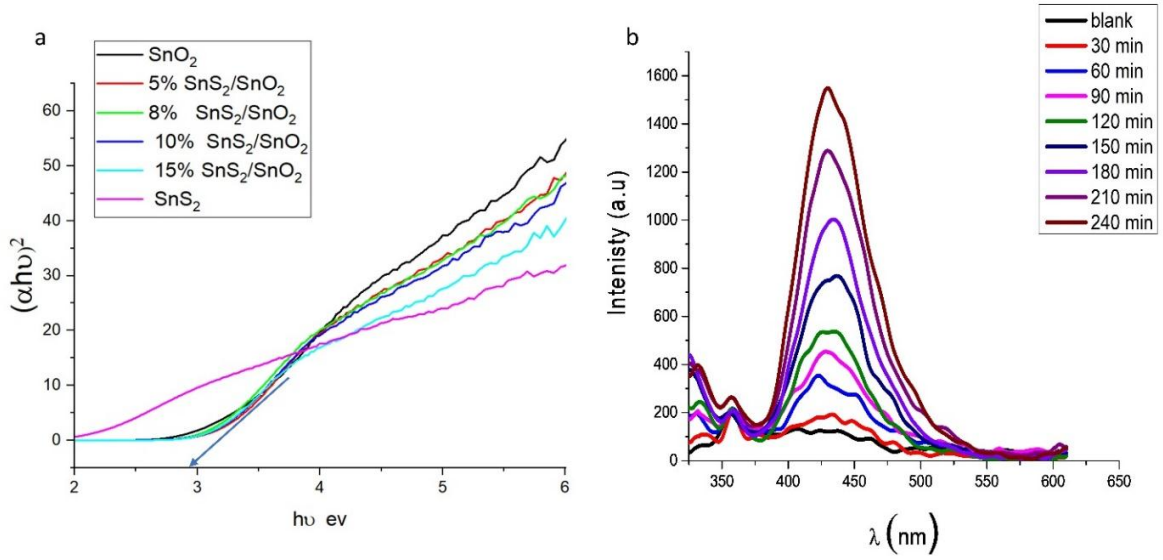

Fig 4: EDX spectrum (a) mapping of elements Oxygen O (b), Sulphur S(c), Tin Sn(d) and over all mapping (e)

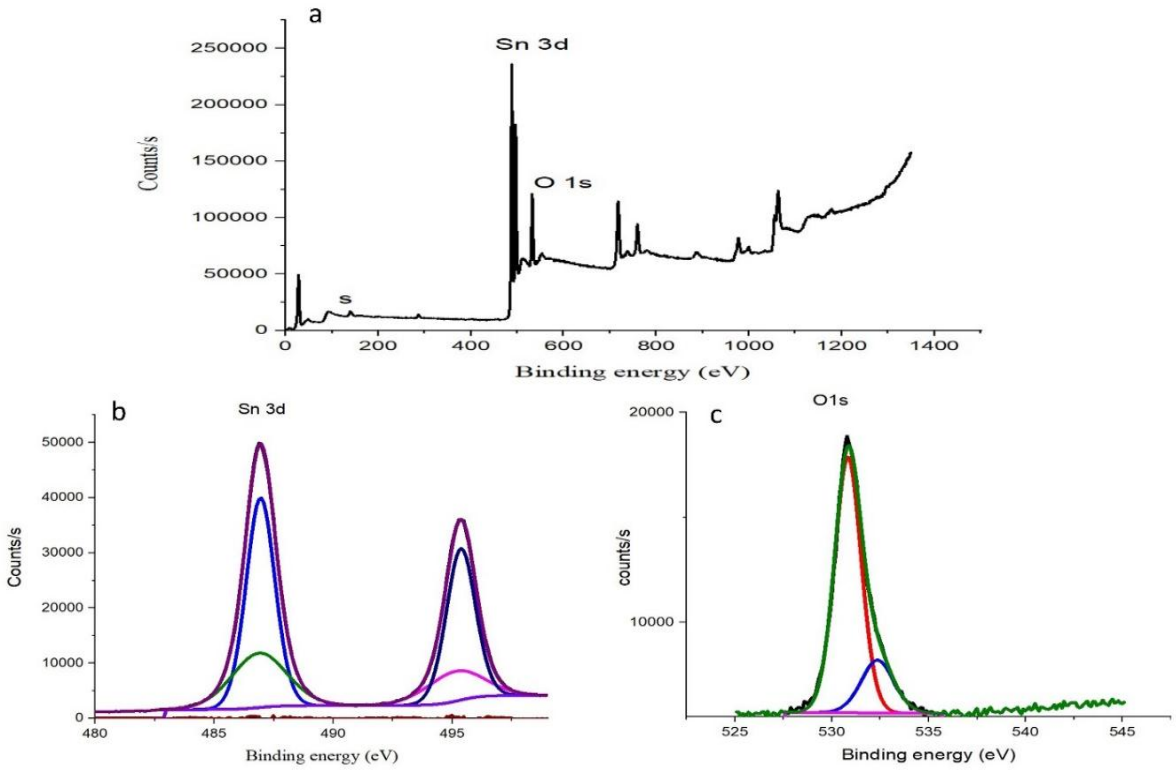

The O 1s spectra of the SnO_2 and SnS_2 materials, as illustrated in Fig. 5(c), reveal two notable binding energies, one at 530 eV and another at 532 eV. These specific binding energies are indicative of oxygen states in the material. The peak at 530 eV is typically associated with the oxygen atoms that are fully coordinated with the tin atoms in the crystalline lattice of SnO_2, i.e., the oxygen atoms in the O^{2-} state. On the other hand, the peak at 532 eV is often linked to oxygen deficiencies in the SnO_2 material, specifically in regions where the oxygen is less coordinated with the tin atoms. This could include adsorbed oxygen species, hydroxyl groups, or oxygen in amorphous regions of the material [33] [34].

Fig 5: XPS spectra of (a). SnS_2/SnO_2, (b) Sn (3d), (c) O (1s)

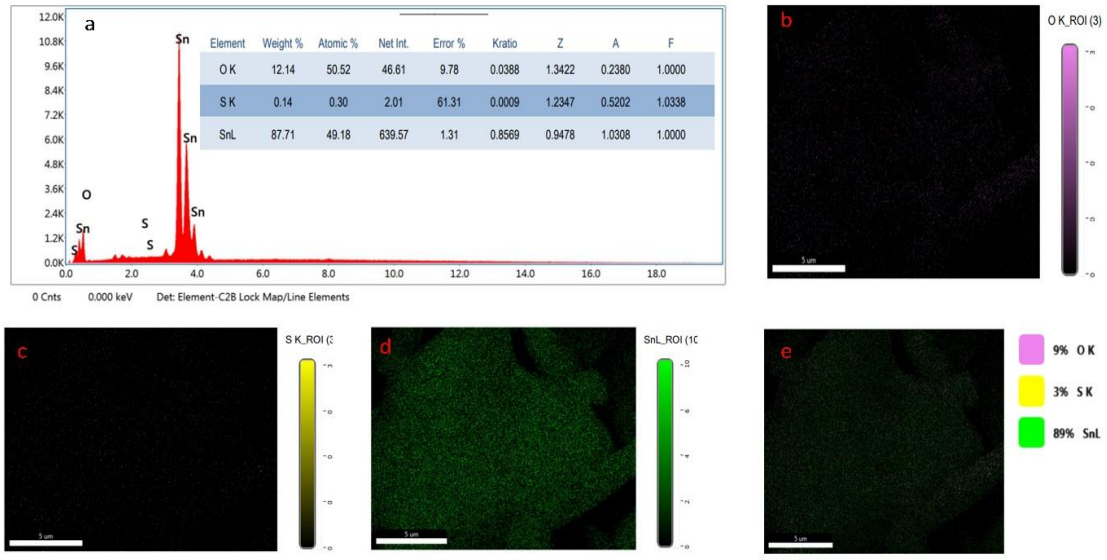

3.3. Photodegradation of fluorescein dye

The photocatalytic performance of the synthesized SnS2/SnO2 nanoparticles was evaluated by examining the photodegradation of fluorescein dye, a representative anionic dye often found in wastewater, under UV-A light irradiation. When fluorescein was exposed solely to UV-A light without the catalyst, its degradation was found to be minimal. However, when both the catalyst and UV irradiation were applied, a substantial improvement was observed, with 61.86% of the fluorescein dye effectively removed within 4 hours.

Photodegradation efficiency, a crucial indicator of the catalyst's effectiveness, is calculated using the formula: Efficiency (%) = $(C_0 - C_t) / C_0 * 100\%$,[35] [36] where C_0 represents the initial concentration of the dye and C_t denotes the dye's concentration at a given time. According to the observations, the SnS_2/SnO_2 nanoparticle catalyst exhibited significant photocatalytic capabilities, promoting an efficiency of 61.86% under UV-A light irradiation over the course of 4 hours. Although promising, further research is needed to fully understand the factors influencing this process, including the catalyst's concentration, the intensity of UV light, and the duration of irradiation.

3.3.1. Effect of pH of the medium .

The absorbance of fluorescein dye is influenced by the pH of the solution, which in turn affects the protolytic form of the dye. The four protolytic forms are cation, neutral, anion, and dianion. Figure 6 depicts the variance in the maximum absorbance wavelength (λmax) of the dye at different pH levels:

At pH 4, the λmax is 454 nm
At pH 6, the λmax is 486 nm
From pH 7 to pH 10, the λmax remains constant at 490 nm
At pH 12, the λmax is 490 nm
The dianion form of the dye, which becomes predominant at higher pH, exhibits a strong absorption at 490 nm and a weaker one at 322 nm. This information is essential as it provides guidance for optimal conditions under which fluorescein dye may be detected and consequently degraded in a photocatalytic process. [37].

3.3.2. Effect of catalyst percent and catalyst dose.

The impact of the catalyst concentration on photodegradation is clearly depicted in Fig. 7. (a-f). The trend suggests that the photodegradation percentage rises with an increase in the catalyst concentration until it reaches a maximum. Beyond this optimal concentration, the photodegradation efficiency starts to decrease. As summarized in Table 1, the highest degradation efficiency was achieved with a catalyst concentration of 0.8 g/L using a 10% SnS_2/SnO_2 blend at a p^H of 7 over a period of four hours. It suggests that any further increase in the catalyst concentration beyond the optimal value leads to a reduction in degradation efficiency, possibly due to the phenomenon of catalyst particle aggregation or increased light scattering, leading to a decrease in light penetration. Therefore, the selection of optimal catalyst concentration is crucial for efficient photodegradation processes.

Fig. 6. Spectrum of fluorescein at various PH.

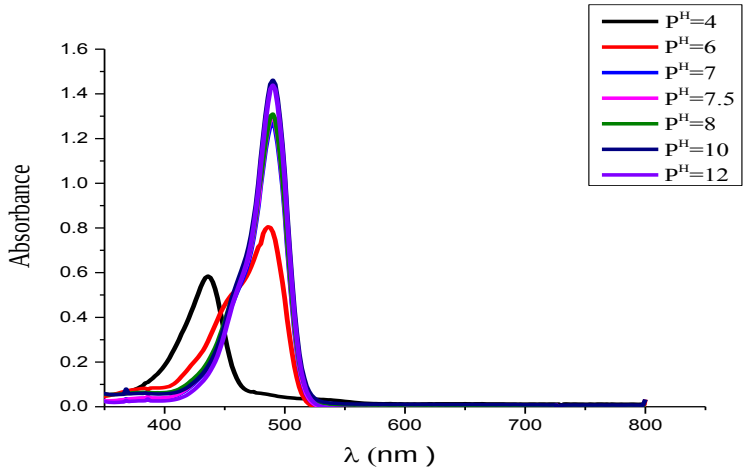

Cat g/L	% SnS_2/SnO_2	$[Flu]_o*10^{-5}$ Mol/L	Initial P^H	Irradiation time H	Removal %
1	0	6	7	4	57.41
1	5	6	7	4	56.69
1	8	6	7	4	53.39
1	10	6	7	4	58.83
1	15	6	7	4	35.07
1	100	6	7	4	5
0.5	10	6	7	4	29.84
0.8	10	6	7	4	77.67
1.5	10	6	7	4	11.45
0.8	10	6	8	4	49.08
0.8	10	6	10	4	18.23

Table 1 Factors affecting photodegradation of fluorescein dye by SnS_2/SnO_2 under UV-A irradiation

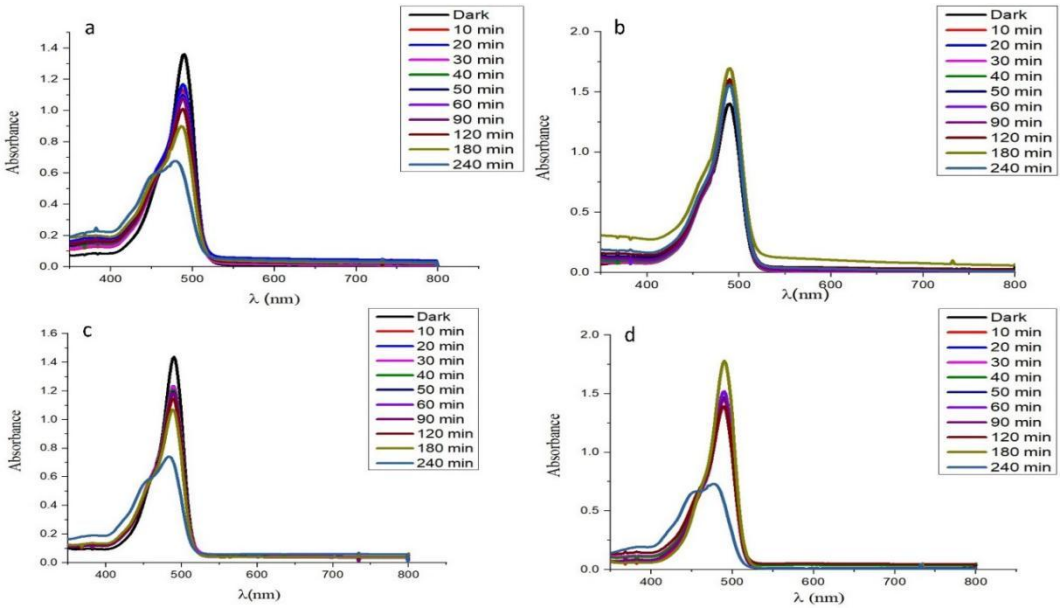

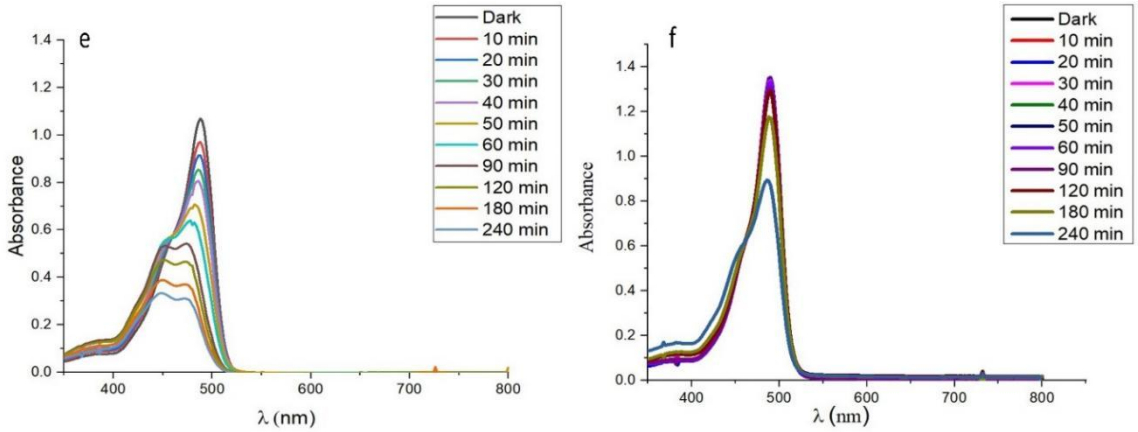

Fig.7: Photodegradation for fluorescein dye (a)SnO_2, (b)SnS_2, (C)5%SnS2/SnO2, (d) 8%SnS_2/SnO_2, (e) 10 %SnS_2/SnO_2, (f) 15% SnS_2/SnO_2 .

3.3.3. Effect of scavenger.

Scavengers are substances used in photocatalytic experiments to trap certain reactive species and thus help determine which species are responsible for the photocatalytic activity. In your research, four different scavengers were used, namely silver nitrate ($AgNO_3$), p-benzoquinone, isopropanol, and ammonium oxalate. Each of these scavengers targets a specific reactive species in the photodegradation process: $AgNO_3$ traps electrons (e^-), p-benzoquinone traps superoxide ions (O^{2-}), isopropanol traps hydroxyl radicals (OH^-), and ammonium oxalate traps positive holes (h^+). The results depicted in Fig. 8 suggest that the photodegradation process is influenced by the presence of these scavengers. Most notably, ammonium oxalate and p-benzoquinone were found to be the most active scavengers, significantly reducing the rate of photodegradation. This indicates that the positive holes (h^+), superoxide ions (O^{2-}), and hydroxyl radicals (OH^-) are key reactive species in the photodegradation process of fluorescein dye under the given experimental conditions. This insight into the primary reactive species can help refine the design and optimization of the photocatalyst system, targeting these reactive species to maximize photodegradation efficiency. [38]

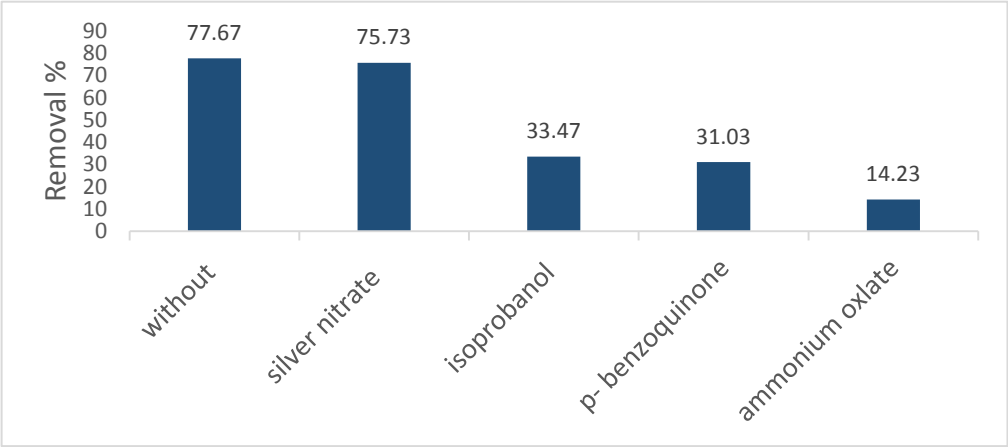

Fig. 8. Effect of scavenger on the removal % of fluorescein.

3.3.4. Recycling of photocatalyst

To assess the stability of the synthesized SnS_2/SnO_2 nanoparticles, a series of photocatalytic cycles were conducted under optimal conditions. After each cycle, the photocatalyst was thoroughly washed with hot distilled water to dislodge any physisorbed dye, and subsequently dried at 100 °C for reuse in the following cycle. As illustrated in Fig. 9, the photocatalytic activity remained largely unchanged through four cycles, indicating the potential of the SnS_2/SnO_2 nanoparticles for repeated usage with consistent efficiency. Consequently, these

nanoparticles present a promising solution for multiple wastewater treatment applications.

3.4. Photocatalytic degradation mechanism

The photocatalytic efficiency of semiconductor materials is predominantly determined by factors such as their surface area, adsorption capacity, and the lifetime of electron-hole (e^-/h^+) separation. The photocatalytic process relies on positive holes (h^+), superoxide radicals ($O.^{-2}$), and hydroxyl radicals ($OH^•$), with the most significant contributors being h^+ and $O.^{-2}$, as shown in the scavenger test. The impact of electrons (e^-) appears to be less substantial in this context.

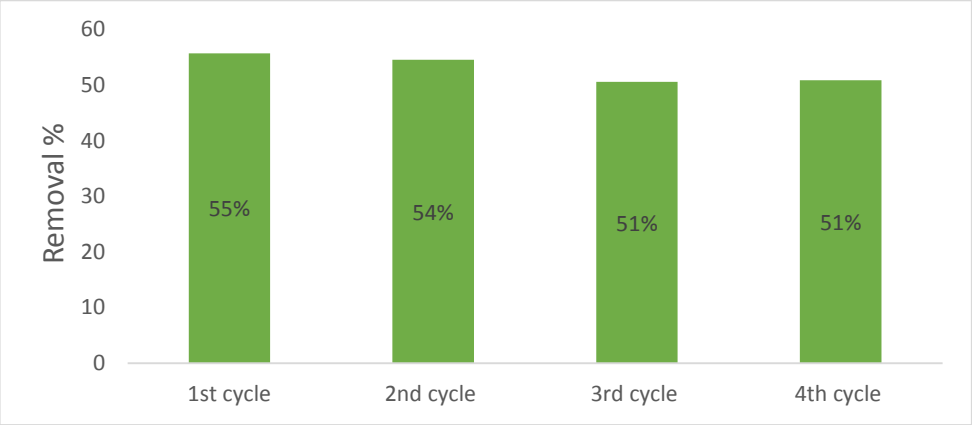

Fig. 9. Photocatalytic efficiency of SnO_2/SnS_2 catalyst toward photodegradation of fluorescein after four cycles.

Additionally, equations 3 and 4 [39] [40] [41] [42] [43] can be employed to calculate the band edge coordinates of VB and CB in nanoparticles.

$$E_{VB} = \chi - E_c + 1/2E_g \quad (3)$$

$$E_{CB} = E_{VB} - E_g \quad (4)$$

In this context, χ represents the absolute electronegativity, which is 6.15 eV for SnO_2 [44] and 4.66 eV for SnS_2 [45]. Ec represents the energy of free electrons on a hydrogen scale and is equal to 4.5 eV. By using equations (4) and (5), we can ascertain the valence band (E_{VB}) and conduction band (E_{CB}) of SnO_2 to be 3.15 eV and 0.15 eV respectively [46]. For SnS_2, these values are found to be 1.095 eV and -0.895 eV respectively [47]. Fig. 10 illustrates a plausible mechanism for the photocatalytic degradation of dye through the Z-scheme mechanism.

The band edge positions of the valence band (VB) and the conduction band (CB) of nanoparticles can be approximated using the Mulliken electronegativity theory, as depicted in equations 3 and 4.

Upon exposure to UV or sunlight radiation, electrons in the conduction band of SnO_2 (with a conduction band potential of =0.15 eV) transfer to the valence band of SnS_2 (with a potential of =1.095 eV). Concurrently, the high reducing and oxidizing power of SnO_2 sustains the positive holes in its valence band (E_{VB}=+3.15 eV) and the electrons in SnS_2's conduction band (E_{CB}=-0.895 eV). The potential of the free positive holes in SnO_2 (E_{VB}=+3.15 eV) is higher than the oxidation potential of H2O/OH, facilitating the generation of hydroxyl radicals a clear indication of the Z-scheme process. Moreover, the production of superoxide radicals is favored when both E_{VB} =+2.88 eV and E_{CB} for SnS_2 =-0.895 eV are more negative than the superoxide ion potential ($EO_2/O_2^·$ =-0.34 eV). This Z-scheme ultimately promotes the rapid degradation of organic pollutants, enhancing the overall photocatalytic process.

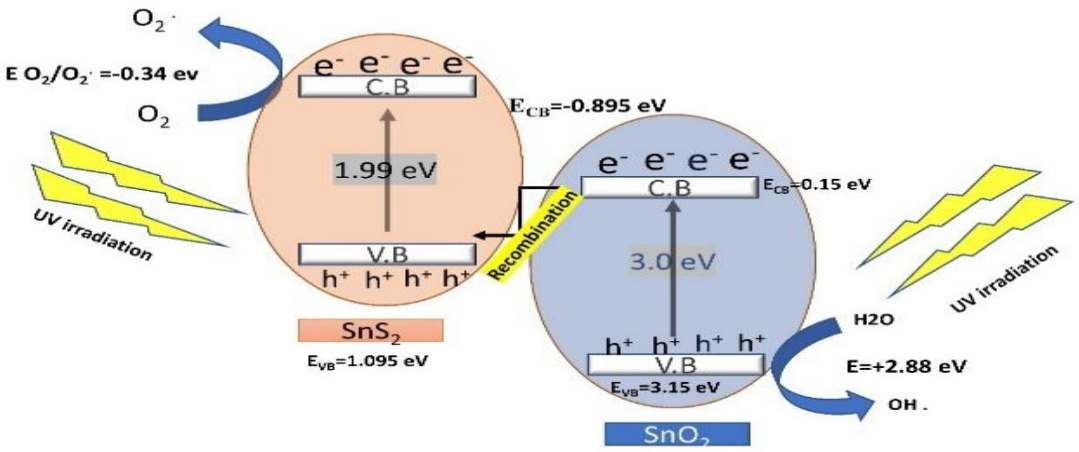

Fig.10. Z-scheme diagram for possible photodegradation mechanism of SnS_2/SnO_2 composite photocatalysts under UV irradiation.

4. Conclusion.

This study has successfully demonstrated the efficacy of an aqueous sol-gel approach in the synthesis of SnS_2/SnO_2 nanostructures. A comprehensive examination of the physicochemical properties of the sample was conducted, employing techniques such as XRD, SEM, TEM, XPS, DRS, PL, BET, and EDX. The successful synthesis of the SnS_2/SnO_2 nanostructures was confirmed through XRD and EDX analyses. XPS analysis further revealed that the synthesized SnS_2/SnO_2 nanocatalyst is oxygen-deficient. A decrease in PL intensity indicates enhanced photocatalytic efficiency. Under UV-A light irradiation, the SnS_2/SnO_2 photocatalyst demonstrated remarkable activity towards the degradation of fluorescein. Several factors were examined for their influence on photocatalytic activity, such as pH, initial catalyst dosage, and SnS_2 percentage on SnO_2. These factors significantly improved the oxidizing and reducing power of holes and electrons. Scavengers and PL results suggest that the primary reactive species responsible for dye degradation are positive holes, hydroxyl radicals, and superoxide radicals. Importantly, the synthesized hybrid nanoparticles retained their reactivity even after four cycles, pointing towards their potential for repeated use in wastewater treatment applications.

5. Acknowledgment

This work was supported by BUE Young Investigator Research Grants (YIRG20-10) at the British university in Egypt

6. References.

[1] K. M. Reza, A. Kurny, and F. Gulshan, “Parameters affecting the photocatalytic degradation of dyes using TiO2: a review,” *Appl. Water Sci.*, vol. 7, no. 4, pp. 1569–1578, 2017, doi: 10.1007/s13201-015-0367-y.

[2] P. Mondal, C. B. Majumder, and B. Mohanty, “Laboratory based approaches for arsenic remediation from contaminated water: Recent developments,” *J. Hazard. Mater.*, vol. 137, no. 1, pp. 464–479, 2006, doi: 10.1016/j.jhazmat.2006.02.023.

[3] I. A. Saleh, N. Zouari, and M. A. Al-Ghouti, “Removal of pesticides from water and wastewater: Chemical, physical and biological treatment approaches,” *Environ. Technol. Innov.*, vol. 19, p. 101026, 2020, doi: 10.1016/j.eti.2020.101026.

[4] R. Al-Tohamy *et al.*, “A critical review on the treatment of dye-containing wastewater: Ecotoxicological and health concerns of textile dyes and possible remediation approaches for environmental safety,” *Ecotoxicol. Environ. Saf.*, vol. 231, p. 113160, 2022, doi: 10.1016/j.ecoenv.2021.113160.

[5] X. Li, J. Yu, S. Wageh, A. A. Al-Ghamdi, and J. Xie, “Graphene in Photocatalysis: A Review,” *Small*, vol. 12, no. 48, pp. 6640–6696, 2016, doi: 10.1002/smll.201600382.

[6] Y. Lan, Y. Lu, and Z. Ren, “Mini review on photocatalysis of titanium dioxide nanoparticles and their solar applications,” *Nano Energy*, vol. 2, no. 5, pp. 1031–1045, 2013, doi: 10.1016/j.nanoen.2013.04.002.

[7] Y. Boyjoo, H. Sun, J. Liu, V. K. Pareek, and S. Wang, “A review on photocatalysis for air treatment: From catalyst development to reactor design,” *Chem. Eng. J.*, vol. 310, pp.

537–559, 2017, doi: 10.1016/j.cej.2016.06.090.

[8] N. S. Andryushina and O. L. Stroyuk, "Influence of colloidal graphene oxide on photocatalytic activity of nanocrystalline TiO2 in gas-phase ethanol and benzene oxidation," *Appl. Catal. B Environ.*, vol. 148–149, pp. 543–549, 2014, doi: 10.1016/j.apcatb.2013.11.044.

[9] T. Kasparek and O. E. Rodriguez, "What medical directors need to know about dialysis facility water management," *Clin. J. Am. Soc. Nephrol.*, vol. 10, no. 6, pp. 1061–1071, 2015, doi: 10.2215/CJN.11851214.

[10] G. Pontoriero, P. Pozzoni, S. Andrulli, and F. Locatelli, "The quality of dialysis water," *Nephrol. Dial. Transplant.*, vol. 18, no. SUPPL. 7, pp. 21–25, 2003, doi: 10.1093/ndt/gfg1074.

[11] L. F. Greenlee, D. F. Lawler, B. D. Freeman, B. Marrot, and P. Moulin, "Reverse osmosis desalination: Water sources, technology, and today's challenges," *Water Res.*, vol. 43, no. 9, pp. 2317–2348, 2009, doi: 10.1016/j.watres.2009.03.010.

[12] A. H. Alneyadi, M. A. Rauf, and S. S. Ashraf, "Oxidoreductases for the remediation of organic pollutants in water–a critical review," *Crit. Rev. Biotechnol.*, vol. 38, no. 7, pp. 971–988, 2018, doi: 10.1080/07388551.2017.1423275.

[13] D. Vuono *et al.*, "Modelling of adsorption of textile dyes over multi-walled carbon nanotubes: Equilibrium and kinetic," *Chinese J. Chem. Eng.*, vol. 25, no. 4, pp. 523–532, 2017, doi: 10.1016/j.cjche.2016.10.021.

[14] C. Sun *et al.*, "Recent intensification strategies of SnO2-based photocatalysts: A review," *Chem. Eng. J.*, vol. 427, no. July 2021, p. 131564, 2022, doi: 10.1016/j.cej.2021.131564.

[15] K. Bhuvaneswari, R. D. Bharathi, and T. Pazhanivel, "Silk fibroin linked Zn / Cd-doped SnO 2 nanoparticles to purify the organically polluted water Silk fi broin linked Zn / Cd-doped SnO 2 nanoparticles to purify the organically polluted water," 2018.

[16] N. AbouSeada, M. A. Ahmed, and M. G. Elmahgary, "Synthesis and characterization of novel magnetic nanoparticles for photocatalytic degradation of indigo carmine dye," *Mater. Sci. Energy Technol.*, vol. 5, pp. 116–124, 2022, doi: 10.1016/j.mset.2022.01.001.

[17] G. Kumar, J. Kumar, M. Bag, and R. Kumar Dutta, "Solar light induced photocatalytic process for reduction of hexavalent chromium and degradation of tetracycline and methylene blue by heterostructures made of SnS2 nanoplates surface modified by ZnWO4 nanorods," *Sep. Purif. Technol.*, vol. 292, no. February, p. 121040, 2022, doi: 10.1016/j.seppur.2022.121040.

[18] M. Najjar, H. A. Hosseini, A. Masoudi, A. Hashemzadeh, and M. Darroudi, "Preparation of tin oxide (IV) nanoparticles by a green chemistry method and investigation of its role in the removal of organic dyes in water purification," *Res. Chem. Intermed.*, vol. 46, no. 4, pp. 2155–2168, 2020, doi: 10.1007/s11164-020-04084-0.

[19] M. Honarmand, M. Golmohammadi, and A. Naeimi, "Biosynthesis of tin oxide (SnO2) nanoparticles using jujube fruit for photocatalytic degradation of organic dyes," *Adv. Powder Technol.*, vol. 30, no. 8, pp. 1551–1557, 2019, doi: 10.1016/j.apt.2019.04.033.

[20] M. U. Yousaf, E. Pervaiz, S. Minallah, M. J. Afzal, L. Honghong, and M. Yang, "Tin oxide quantum dots decorated graphitic carbon nitride for enhanced removal of organic components from water: Green process," *Results Phys.*, vol. 14, no. May, p. 102455, 2019, doi: 10.1016/j.rinp.2019.102455.

[21] N. Al-Zaqri, A. Alsalme, M. A. Ahmed, and A. H. Galal, "Construction of novel direct Z-scheme AgIO4-g-C3N4 heterojunction for photocatalytic hydrogen production and photodegradation of fluorescein dye," *Diam. Relat. Mater.*, vol. 109, no. August, p. 108071, 2020, doi: 10.1016/j.diamond.2020.108071.

[22] R. R. Srivastava, P. K. Vishwakarma, U. Yadav, and S. Rai, "2D SnS 2 Nanostructure-Derived Photocatalytic Degradation of Organic Pollutants Under Visible Light," vol. 3, no. August, pp. 1–13, 2021, doi: 10.3389/fnano.2021.711368.

[23] S. Selvi, N. Jayamani, and D. Barathi, "Stannic oxide nanoparticles: sono-synthesis using seed extract of Ziziphus zizyphus and its photocatalytic activity," *J. Mater. Sci. Mater. Electron.*, vol. 32, no. 20, pp. 25433–25443, 2021, doi: 10.1007/s10854-021-07003-0.

[24] N. Rani and N. Jaggi, "Effect of reaction temperature on the structural and electronic properties of stannic oxide nanostructures," *Bull. Mater. Sci.*, vol. 43, no. 1, pp. 1–7, 2020, doi: 10.1007/s12034-020-02141-3.

[25] L. Kong and H. Adidharma, "A new adsorption model based on generalized van der Waals partition function for the description of all types of adsorption isotherms," *Chem. Eng. J.*, vol. 375, no. June, p. 122112, 2019, doi:

10.1016/j.cej.2019.122112.

[26] J. Samuelsson, T. Undin, and T. Fornstedt, "Expanding the elution by characteristic point method for determination of various types of adsorption isotherms," *J. Chromatogr. A*, vol. 1218, no. 24, pp. 3737–3742, 2011, doi: 10.1016/j.chroma.2011.04.035.

[27] B. Ba Mohammed *et al.*, "Adsorptive removal of phenol using faujasite-type Y zeolite: Adsorption isotherms, kinetics and grand canonical Monte Carlo simulation studies," *J. Mol. Liq.*, vol. 296, 2019, doi: 10.1016/j.molliq.2019.111997.

[28] Z. Li, Y. Zhou, W. Mao, and Z. Zou, "Nanowire-based hierarchical tin oxide/zinc stannate hollow microspheres: Enhanced solar energy utilization efficiency for dye-sensitized solar cells and photocatalytic degradation of dyes," *J. Power Sources*, vol. 274, pp. 575–581, 2015, doi: 10.1016/j.jpowsour.2014.10.129.

[29] G. Žerjav, A. Albreht, I. Vovk, and A. Pintar, "Revisiting terephthalic acid and coumarin as probes for photoluminescent determination of hydroxyl radical formation rate in heterogeneous photocatalysis," *Appl. Catal. A Gen.*, vol. 598, no. December 2019, 2020, doi: 10.1016/j.apcata.2020.117566.

[30] J. Huang, Y. Liu, Y. Wu, and X. Li, "Influence of Mn Doping on the Sensing Properties of SnO₂ Nanobelt to Ethanol," *Am. J. Anal. Chem.*, vol. 08, no. 01, pp. 60–71, 2017, doi: 10.4236/ajac.2017.81005.

[31] S. Velmurugan, L. Zhi-Xiang, T. C-K Yang, and J. C. Juan, "Rational design of built-in stannic oxide-copper manganate microrods p-n heterojunction for photoelectrochemical sensing of tetracycline," *Chemosphere*, vol. 271, p. 129788, 2021, doi: 10.1016/j.chemosphere.2021.129788.

[32] J. Su, T. Hsieh, S. Yang, S. Chao, and K. Lu, "Fabrication and Photocatalytic Properties of Zinc Tin Oxide Nanowires Decorated with Silver Nanoparticles," pp. 1–11, 2022.

[33] M. Kwoka, L. Ottaviano, M. Passacantando, S. Santucci, G. Czempik, and J. Szuber, "XPS study of the surface chemistry of L-CVD SnO2 thin films after oxidation," *Thin Solid Films*, vol. 490, no. 1, pp. 36–42, 2005, doi: 10.1016/j.tsf.2005.04.014.

[34] M. Govindasamy, B. Sriram, S. F. Wang, Y. J. Chang, and J. R. Rajabathar, "Highly sensitive determination of cancer toxic mercury ions in biological and human sustenance samples based on green and robust synthesized stannic oxide nanoparticles decorated reduced graphene oxide sheets," *Anal. Chim. Acta*, vol. 1137, pp. 181–190, 2020, doi: 10.1016/j.aca.2020.09.014.

[35] A. Enesca, L. Andronic, and A. Duta, "The influence of surfactants on the crystalline structure, electrical and photocatalytic properties of hybrid multi-structured (SnO 2 , TiO 2 and WO 3) thin films," *Appl. Surf. Sci.*, vol. 258, no. 10, pp. 4339–4346, 2012, doi: 10.1016/j.apsusc.2011.12.110.

[36] E. Abdelkader, L. Nadjia, B. Naceur, and B. Noureddine, "SnO2 foam grain-shaped nanoparticles: Synthesis, characterization and UVA light induced photocatalysis," *J. Alloys Compd.*, vol. 679, pp. 408–419, 2016, doi: 10.1016/j.jallcom.2016.04.016.

[37] A. C. Tella, S. O. Owalude, C. A. Ojekanmi, and O. S. Oluwafemi, "Synthesis of copper-isonicotinate metal-organic frameworks simply by mixing solid reactants and investigation of their adsorptive properties for the removal of the fluorescein dye," *New J. Chem.*, vol. 38, no. 9, pp. 4494–4500, 2014, doi: 10.1039/c4nj00411f.

[38] A. R. Dash *et al.*, "Green Synthesis of Stannic Oxide Nanoparticles for Ciprofloxacin Degradation: Optimization and Modelling Using a Response Surface Methodology (RSM) Based on the Box–Behnken Design," *J. Clust. Sci.*, vol. 0123456789, 2021, doi: 10.1007/s10876-021-02198-y.

[39] M. Alhaddad and M. H. H. Mahmoud, "Enhanced photocatalytic reduction of mercuric cations endorsing fabricated mesoporous BiFeO3/g-C3N4 heterojunction under Vis light irradiation," *Appl. Nanosci.*, vol. 11, no. 2, pp. 621–635, 2021, doi: 10.1007/s13204-020-01607-4.

[40] K. S. Al-Namshah and R. M. Mohamed, "Development of mesoporous Bi2WO6/g-C3N4 heterojunctions via soft- and hard-template-assisted procedures for accelerated and reinforced photocatalytic reduction of mercuric cations under vis light irradiation," *Ceram. Int.*, vol. 47, no. 4, pp. 5003–5012, 2021, doi: 10.1016/j.ceramint.2020.10.076.

[41] F. Duo, Y. Wang, X. Mao, X. Zhang, Y. Wang, and C. Fan, "A BiPO 4 /BiOCl heterojunction photocatalyst with enhanced electron-hole separation and excellent photocatalytic performance," *Appl. Surf. Sci.*, vol. 340, pp. 35–42, 2015, doi: 10.1016/j.apsusc.2015.02.175.

[42] A. H. Galal, M. G. Elmahgary, and M. A. Ahmed, "Construction of novel AgIO4/ZnO/graphene direct Z-scheme

heterojunctions for exceptional photocatalytic hydrogen gas production," *Nanotechnol. Environ. Eng.*, vol. 6, no. 1, pp. 1–10, 2021, doi: 10.1007/s41204-020-00096-8.

[43] K. Anandan, K. Rajesh, K. Gayathri, S. Vinoth Sharma, S. G. Mohammed Hussain, and V. Rajendran, "Effects of rare earth, transition and post transition metal ions on structural and optical properties and photocatalytic activities of zirconia (ZrO2) nanoparticles synthesized via the facile precipitation process," *Phys. E Low-Dimensional Syst. Nanostructures*, vol. 124, no. June, p. 114342, 2020, doi: 10.1016/j.physe.2020.114342.

[44] M. A. Ahmed, A. Fahmy, M. G. Abuzaid, and E. M. Hashem, "Fabrication of novel AgIO4/SnO2 heterojunction for photocatalytic hydrogen production through direct Z-scheme mechanism," *J. Photochem. Photobiol. A Chem.*, vol. 400, no. May, p. 112660, 2020, doi: 10.1016/j.jphotochem.2020.112660.

[45] X. Li, J. Zhu, and H. Li, "Comparative study on the mechanism in photocatalytic degradation of different-type organic dyes on SnS 2 and CdS," *Appl. Catal. B Environ.*, vol. 123–124, pp. 174–181, 2012, doi: 10.1016/j.apcatb.2012.04.009.

[46] B. Tao and Z. Yan, "In-situ synthesis of highly efficient visible light driven stannic oxide/graphitic carbon nitride heterostructured photocatalysts," *J. Colloid Interface Sci.*, vol. 480, pp. 118–125, 2016, doi: 10.1016/j.jcis.2016.07.009.

[47] Y. Li, B. Yu, Z. Hu, and H. Wang, "Construction of direct Z-scheme SnS2@ZnIn2S4@kaolinite heterostructure photocatalyst for efficient photocatalytic degradation of tetracycline hydrochloride," *Chem. Eng. J.*, vol. 429, no. August 2021, p. 132105, 2022, doi: 10.1016/j.cej.2021.132105.

[48] M. A. Ahmed, B. M. Mahran, A. M. Abbas, M. A. Tarek, and A. M. Saed, "Construction of direct Z-scheme AgIO4/TiO2 heterojunctions for exceptional photodegradation of rhodamine B dye," *J. Dispers. Sci. Technol.*, vol. 43, no. 3, pp. 349–363, 2022, doi: 10.1080/01932691.2020.1841652.